Energy &
Environmental
Science

COMMUNICATION

Cite this: *Energy Environ. Sci.*, 2018, **11**, 1204

Received 15th January 2018,
Accepted 19th March 2018

DOI: 10.1039/c8ee00133b

rsc.li/ees

Coordinatively unsaturated nickel–nitrogen sites towards selective and high-rate CO_2 electroreduction†

Chengcheng Yan,‡[ab] Haobo Li,‡[ab] Yifan Ye,[ab] Haihua Wu,[ab] Fan Cai,[ab] Rui Si,[c] Jianping Xiao,[a] Shu Miao,[a] Songhai Xie,[d] Fan Yang,[a] Yanshuo Li,[e] Guoxiong Wang *[a] and Xinhe Bao *[a]

High Faradaic efficiency and appreciable current density are essential for future applications of the electrochemical CO_2 reduction reaction (CO_2RR). However, these goals are difficult to achieve simultaneously due to the severe side reaction – the hydrogen evolution reaction (HER). Herein, we successfully synthesized coordinatively unsaturated nickel–nitrogen (Ni–N) sites doped within porous carbon with a nickel loading as high as 5.44 wt% by pyrolysis of Zn/Ni bimetallic zeolitic imidazolate framework-8. Over the Ni–N composite catalysts, the CO current density increases with the overpotential and reaches 71.5 ± 2.9 mA cm^{-2} at −1.03 V (*vs.* a reversible hydrogen electrode, RHE), while maintaining a high CO Faradaic efficiency of 92.0–98.0% over a wide potential range of −0.53 to −1.03 V (*vs.* the RHE). Density functional theory calculations suggest that the CO_2RR occurs more easily than the HER over the coordinatively unsaturated Ni–N site. Therefore, highly doped and coordinatively unsaturated Ni–N sites achieve high current density and Faradaic efficiency of the CO_2RR simultaneously, breaking current limits in metal–nitrogen composite catalysts.

The electrochemical CO_2 reduction reaction (CO_2RR) is a potentially effective approach to achieve intermittent renewable electricity storage and CO_2 conversion simultaneously.[1–3] An efficient catalyst must inhibit the hydrogen evolution reaction (HER) while enhancing CO_2RR activity.[4–6] Recently, metal–nitrogen active sites embedded in carbon have demonstrated impressive Faradaic efficiencies for the CO_2RR.[7–12] However, the partial current densities of the CO_2RR over these metal–nitrogen composite catalysts are usually limited. Typically, the Faradaic efficiencies of the CO_2RR drop rapidly, accompanying an increase in the overpotential in order to achieve high current densities.[7–12] So far, metal–nitrogen composite catalysts have suffered the problem of achieving high current density while maintaining high Faradaic efficiency for the CO_2RR, which is essential for the requirements of fast reaction rate and high reaction selectivity in future applications of the CO_2RR.

Herein, we propose a strategy to facilitate the CO_2RR through the construction of coordinatively unsaturated nickel–nitrogen (Ni–N) active sites within porous carbon, derived from the pyrolysis of Zn/Ni bimetallic zeolitic imidazolate framework-8 (ZIF-8), with a Ni loading as high as 5.44 wt%. The CO Faradaic efficiency is maintained between 92.0% and 98.0% over a wide potential range of −0.53 V to −1.03 V (*vs.* the reversible hydrogen electrode, RHE), while the CO current density increases with the overpotential and reaches an unprecedentedly high value of 71.5 ± 2.9 mA cm^{-2} at −1.03 V (*vs.* RHE). Density functional theory (DFT) calculations suggest that the CO_2RR occurs more easily than the HER over the coordinatively unsaturated Ni–N site. Thus, both high Faradaic efficiency and current density of the CO_2RR are achieved simultaneously.

Fig. 1a shows the preparation scheme of Zn/Ni bimetallic ZIF-8 and its subsequent pyrolysis product (synthesis procedures are detailed in the experimental section).[13] Zn/Ni bimetallic ZIF-8 with different ratios of Zn to Ni was prepared by varying the concentration of $Zn(NO_3)_2$ and $Ni(NO_3)_2$ in methanol, denoted as Zn_xNi_y ZIF-8, according to the molar ratio of Zn to Ni in the precursor solution. With an increase in the percentage of Ni, the Zn_xNi_y ZIF-8 nanoparticles (NPs) retain a similar crystalline structure (Fig. S1, ESI†), while the color gradually changes from white to dark violet (Fig. S2, ESI†). The content of Ni in the Zn_xNi_y ZIF-8 NPs increases with the concentration of Ni in the precursor solution as measured by inductively coupled plasma optical emission spectroscopy (ICP-OES, Table S1, ESI†). ZIF-8, Zn_2Ni_1 ZIF-8 and Zn_1Ni_1 ZIF-8 NPs were then pyrolyzed under an

---

[a] *State Key Laboratory of Catalysis, CAS Center for Excellence in Nanoscience, Dalian National Laboratory for Clean Energy, Dalian Institute of Chemical Physics, Chinese Academy of Sciences, Dalian, 116023, China. E-mail: wanggx@dicp.ac.cn, xhbao@dicp.ac.cn*

[b] *University of Chinese Academy of Sciences, Beijing, 100039, China*

[c] *Shanghai Synchrotron Radiation Facility, Shanghai Institute of Applied Physics, Chinese Academy of Sciences, Shanghai, 201204, China*

[d] *Shanghai Key Laboratory of Molecular Catalysis and Innovative Materials, Department of Chemistry, Fudan University, Shanghai, 200433, China*

[e] *School of Material Science and Chemical Engineering, Department of Chemistry, Ningbo University, Ningbo, 315211, China*

† Electronic supplementary information (ESI) available. See DOI: 10.1039/c8ee00133b

‡ These authors have contributed equally.

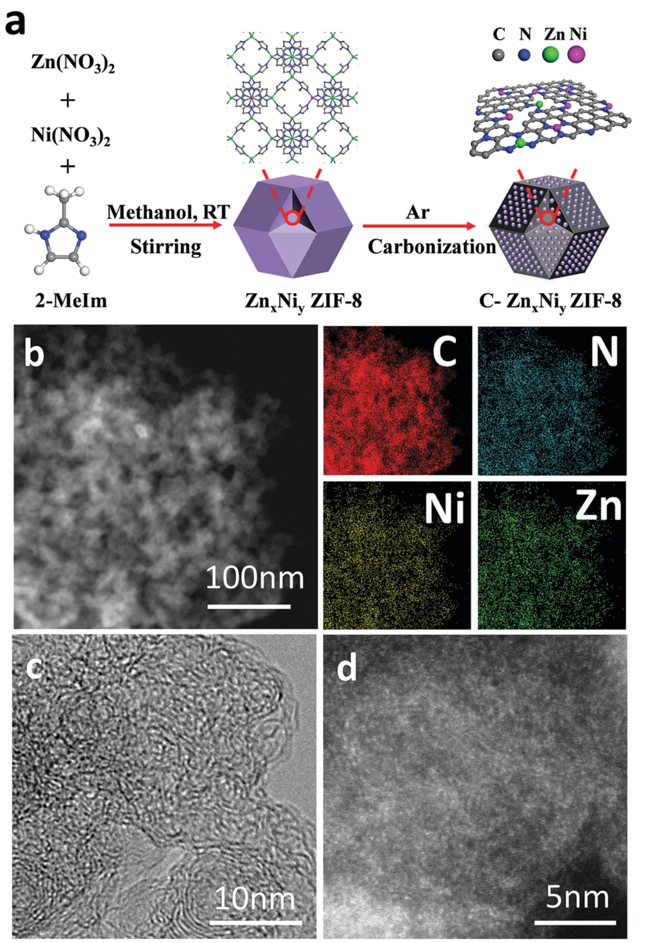

Fig. 1 (a) Schematic illustration of the synthesis of C-Zn$_x$Ni$_y$ ZIF-8, (b) low-resolution HAADF-STEM image of C-Zn$_1$Ni$_4$ ZIF-8 and the corresponding EDS images for C, N, Ni, and Zn in C-Zn$_1$Ni$_4$ ZIF-8, (c) HRTEM and (d) high-resolution HAADF-STEM images of C-Zn$_1$Ni$_4$ ZIF-8.

Ar atmosphere at 1000 °C for 4 h, and the pyrolysis products were denoted as C-ZIF-8, C-Zn$_2$Ni$_1$ ZIF-8 and C-Zn$_1$Ni$_1$ ZIF-8, respectively. To prevent the formation of Ni NPs for a high Ni content during pyrolysis, Zn$_1$Ni$_4$ ZIF-8 was pyrolyzed under an Ar atmosphere at 900 °C for 10 h, and the pyrolysis product was denoted as C-Zn$_1$Ni$_4$ ZIF-8. Low-resolution high-angle annular dark field-scanning transmission electron microscopy (HAADF-STEM) images with the corresponding energy dispersive X-ray spectroscopy (EDS) images show that the elements of Ni, Zn, N and C are uniformly distributed in C-Zn$_1$Ni$_4$ ZIF-8 (Fig. 1b). Backscattered scanning electron microscopy images of the pyrolysis products (C-Zn$_2$Ni$_1$ ZIF-8, C-Zn$_1$Ni$_1$ ZIF-8 and C-Zn$_1$Ni$_4$ ZIF-8) in Fig. S3, ESI† show no bright spots, thus excluding the existence of metal NPs.[14] High-resolution TEM (HRTEM) images in different regions of C-Zn$_1$Ni$_4$ ZIF-8 (Fig. 1c and Fig. S4, ESI†) show porous graphitic carbon in the absence of metal NPs. And the corresponding selected area electron diffraction (SAED) patterns show mere characteristic diffraction of carbon.[15,16] Furthermore, high-resolution HAADF-STEM images in Fig. 1d and Fig. S5, ESI† show the atomic dispersion of metal species and no existence of metal NPs in C-Zn$_1$Ni$_4$ ZIF-8. C-Zn$_2$Ni$_1$ ZIF-8 and C-Zn$_1$Ni$_1$ ZIF-8 also show similar morphologies and atomic dispersions of metal species in the absence of metal NPs (Fig. S6, ESI†).

The pyrolysis products derived from Zn$_x$Ni$_y$ ZIF-8 show similar XRD patterns and no diffraction peaks, which indicates the absence of Ni and Zn NPs (Fig. 2a), in agreement with the SEM, HRTEM and HAADF-STEM results. The Ni 2p XPS spectra of the pyrolysis products and nickel phthalocyanine (NiPc) are displayed in Fig. 2b. All binding energies of the Ni 2p$_{3/2}$ peak in the pyrolysis products are around 855.0 eV, higher than that of metallic Ni^0 (~853.0 eV)[17] and lower than that of Ni^{2+} in NiPc (~855.7 eV),[18] indicative of a valence of Ni species between 0 and +2. The Ni 2p intensity increases from C-Zn$_2$Ni$_1$ ZIF-8 to C-Zn$_1$Ni$_4$ ZIF-8 due to enhanced Ni loading (Table S2, ESI†). The N 1s signal band (Fig. S7, ESI†) of all the pyrolysis products is split into five nitrogen configurations, originating from pyridinic–N (398.3 ± 0.2 eV), metal–N (399.6 ± 0.2 eV), pyrrolic–N (400.8 ± 0.2 eV), graphitic–N (402.2 ± 0.2 eV) and oxidized–N (>404.0 eV), respectively.[10,19,20] Table S3, ESI† shows the ratio of different nitrogen configurations. The presence of metal–N suggests that these nitrogen atoms bind to Ni or Zn atoms directly, and the binding energy of metal–N is similar to that of Ni–N in NiPc.[21] The Ni K edge X-ray absorption near edge structure (XANES) and extended X-ray absorption fine structure (EXAFS) of C-Zn$_x$Ni$_y$ ZIF-8 compared with those of standard Ni foil and NiPc are shown in Fig. 2c and d. Both the Ni absorption edge and main transition energies of C-Zn$_2$Ni$_1$ ZIF-8, C-Zn$_1$Ni$_1$ ZIF-8 and C-Zn$_1$Ni$_4$ ZIF-8 are between those of Ni foil and NiPc, suggesting that Ni in the pyrolysis products is in intermediate valence states. Fourier transformed EXAFS analysis also confirms the presence of Ni–N bonds and the absence of Ni–Ni bonds in the pyrolysis products, indicating that the Ni atoms are atomically dispersed and bonded with N atoms in the samples, in agreement with the HAADF-STEM results (Fig. 1d).[22,23] The fitting results from EXAFS analysis in Fig. 2d and Table S4, ESI† show that the coordination numbers of Ni species in C-Zn$_2$Ni$_1$ ZIF-8, C-Zn$_1$Ni$_1$ ZIF-8 and C-Zn$_1$Ni$_4$ ZIF-8 are 2.6 ± 0.4, 2.7 ± 0.4, and 2.4 ± 0.4, respectively, revealing the coordinatively unsaturated state of the Ni species. Similar to the characterization of the Ni species, XANES and EXAFS results (Fig. S8, ESI†) also indicate that the Zn species are atomically dispersed and bonded with N atoms. The coordination numbers of Zn species in C-ZIF-8, C-Zn$_2$Ni$_1$ ZIF-8, C-Zn$_1$Ni$_1$ ZIF-8 and C-Zn$_1$Ni$_4$ ZIF-8 are fitted to be 3.6 ± 0.6, 3.5 ± 0.7, 3.4 ± 0.8 and 3.5 ± 0.9, respectively (Table S5, ESI†). During the pyrolysis, 2-MeIm was carbonized, while most Zn species were evaporated and the residual coordinated Ni and Zn species were proposed to be anchored into the carbon matrix with N sites. Thus the mixing of Zn not only acts as a spacer to prevent the aggregation of Ni species but also plays an important role in the construction of the porous structure.[16] Notably, different from the commonly-used post-synthetic modification strategy,[8,11] in our work Ni^{2+} ions were doped into the ZIF-8 skeleton by partially replacing Zn^{2+} in the crystallization process as confirmed by the consistency of the XPS and ICP-OES results (Table S2, ESI†), which maximizes the density of atomically dispersed Ni–N$_x$ sites to an

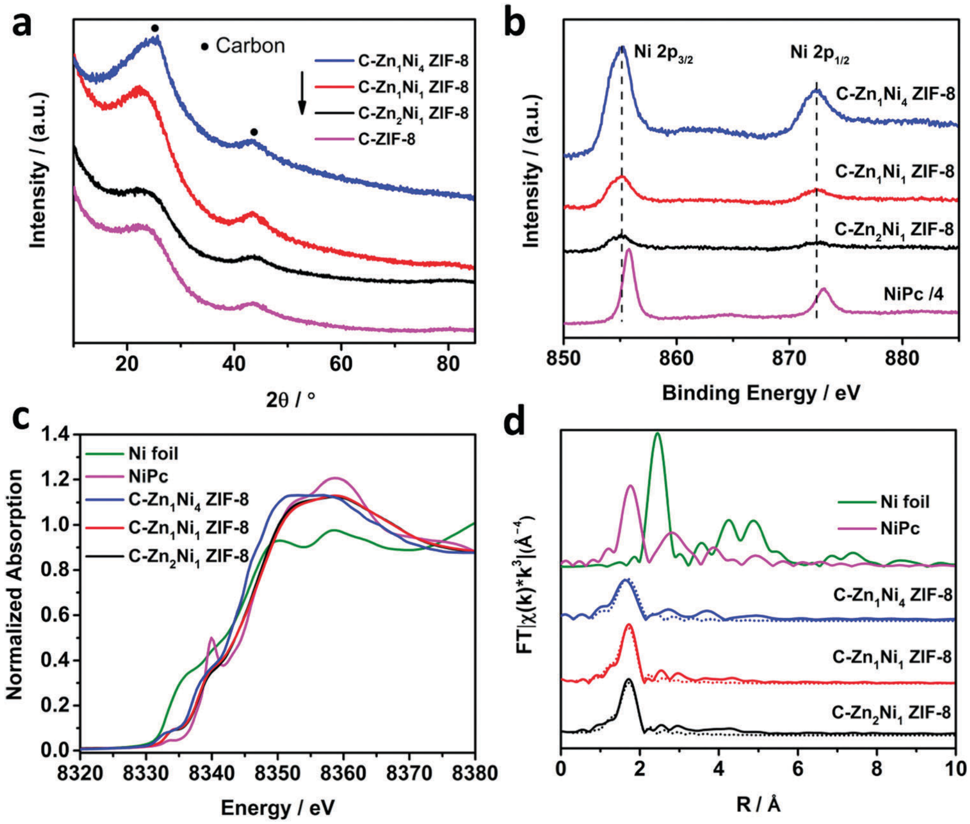

Fig. 2 Characterization of C-Zn_xNi_y ZIF-8. (a) XRD patterns, (b) Ni 2p high-resolution XPS surveys of C-Zn_xNi_y ZIF-8 and NiPc, (c) XANES spectra and (d) Fourier transformed EXAFS spectra of the Ni K-edge for C-Zn_xNi_y ZIF-8 and the corresponding reference samples (solid lines stand for the as obtained data and dotted lines denote the fitting curves).

exceptionally high Ni loading of 5.44 wt%. The specific surface area of the pyrolysis product was measured *via* N_2 adsorption–desorption. All of the pyrolysis products possess high surface areas, despite a small decrease on increasing the Ni concentration in the Zn_xNi_y ZIF-8 precursor and the pore size distribution remains unchanged (Fig. S9 and Table S6, ESI†). Besides, the CO_2 adsorption isotherms of these pyrolysis products show considerable capacity for CO_2 adsorption at room temperature (Fig. S10, ESI†).

The selectivity and reaction rate of the pyrolysis products towards the CO_2RR were evaluated by controlled-potential electrolysis in an H-cell filled with a CO_2-saturated $KHCO_3$ solution (see the Experimental section for details, Fig. S11, ESI†). The catalysts show stable time-dependent total current densities at different applied potentials (Fig. S12, ESI†). CO and H_2 are the only two detected gas products (Fig. S13, ESI†), quantified by on-line micro gas chromatography, and no liquid products in the cathodic electrolyte after the CO_2RR measurements were detected by nuclear magnetic resonance spectroscopy (Fig. S14, ESI†). In the CO_2-saturated 1 M $KHCO_3$ solution, C-ZIF-8 shows the poorest CO_2RR activity, with a maximum CO Faradaic efficiency of 20.0% and low current density at even high overpotentials, indicating that the Zn–N sites have poor selectivity and activity for the CO_2RR. C-Zn_2Ni_1 ZIF-8, C-Zn_1Ni_1 ZIF-8 and C-Zn_1Ni_4 ZIF-8 show much enhanced CO Faradaic efficiencies compared with C-ZIF-8, as shown in Fig. 3a. In particular, the CO Faradaic efficiencies over C-Zn_1Ni_1 ZIF-8 and C-Zn_1Ni_4 ZIF-8 exceed 92.0% over the potential range of −0.53 to −1.03 V (*vs.* the RHE) and the HER was severely inhibited as shown in Fig. S15 and Table S7, ESI.† For comparison, NiPc was also used to catalyze the CO_2RR, and CO was generated over NiPc at −0.63 V (*vs.* the RHE) with a Faradaic efficiency of 77.0%, but decreased sharply with increasing overpotentials. Fig. 3b shows the dependence of the CO current density on applied potential. C-ZIF-8 and NiPc demonstrate a very low CO current density, probably due to the lack of coordinatively unsaturated Ni–N sites. All C-Zn_xNi_y ZIF-8 catalysts show a high CO current density, which increases with the applied potential and reaches 71.5 ± 2.9 mA cm^{-2} at −1.03 V (*vs.* the RHE) over C-Zn_1Ni_4 ZIF-8.

In CO_2-saturated 0.1 M and 0.5 M $KHCO_3$ solutions (Fig. S16, ESI†), the CO Faradaic efficiencies over C-Zn_1Ni_4 ZIF-8 also remain stable between 90.0–98.0% and the current density increases with the overpotential over the potential range of −0.63 V to −1.03 V (*vs.* the RHE). Thus, C-Zn_1Ni_4 ZIF-8 achieves a high current density and Faradaic efficiency of the CO_2RR simultaneously, distinguished from those of the CO_2RR over the reported Fe–N and Ni–N composite catalysts.[7–12] As shown in Fig. S17, ESI,† C-Zn_1Ni_4 ZIF-8 shows a high CO Faradaic efficiency and CO current density among recently reported representative noble metal catalysts and metal–nitrogen composite catalysts.

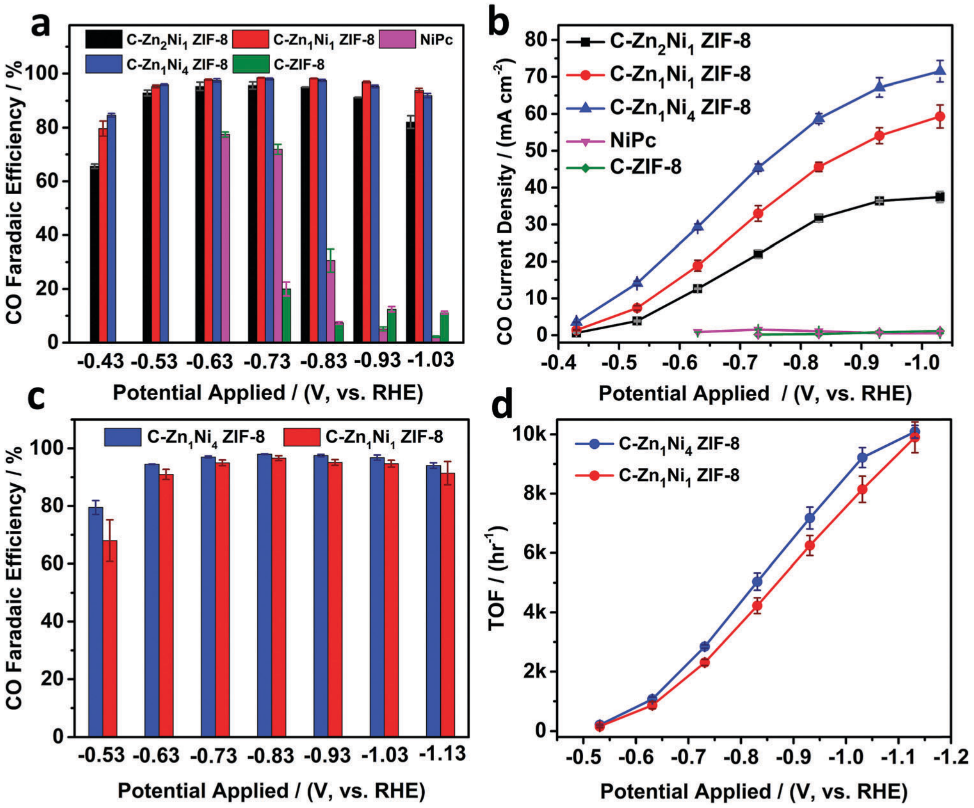

Fig. 3 Electrocatalytic performances of the CO_2RR over the catalysts. (a) Applied potential dependence of CO Faradaic efficiency, (b) CO partial current density measured in CO_2-saturated 1 M $KHCO_3$ solution with a catalyst loading of 2.0 ± 0.1 mg cm^{-2} for C-Zn$_x$Ni$_y$ ZIF-8 and 1.06 mg cm^{-2} for NiPc. (c) Applied potential dependence of CO Faradaic efficiency, and (d) calculated TOF at different potentials measured in CO_2-saturated 0.5 M $KHCO_3$ solution with a catalyst loading of 0.088 mg cm^{-2} for C-Zn$_1$Ni$_4$ ZIF-8 and 0.226 mg cm^{-2} for C-Zn$_1$Ni$_1$ ZIF-8.

Furthermore, we quantified the specific activities of the pyrolysis products according to the calculated value of turnover frequency (TOF, calculation details in the Experimental section, ESI†). The C-Zn$_1$Ni$_4$ ZIF-8 and C-Zn$_1$Ni$_1$ ZIF-8 electrodes with a lower catalyst loading (0.088 mg cm^{-2} and 0.226 mg cm^{-2}, respectively, to guarantee the same Ni loading on the electrode) were used to make sure that all of the painted catalysts were involved in the CO_2RR. For comparison with other atomically dispersed Ni catalysts, CO_2RR tests were carried out in CO_2-saturated 0.5 M $KHCO_3$ solution and the results are shown in Fig. 3c, d and Fig. S15, S18, Table S7 ESI.† At the low catalyst loading, the CO Faradaic efficiency still remains between 90.0% and 98.0% over a wide potential range between −0.53 V and −1.13 V (*vs.* the RHE). C-Zn$_1$Ni$_4$ ZIF-8 and C-Zn$_1$Ni$_1$ ZIF-8 exhibit similar TOF and the same uptrend in the whole potential range, suggesting the same active sites for the CO_2RR in the pyrolysis products. The TOF increases with the overpotential and reaches an extremely high value of 10087 ± 216 h^{-1} for C-Zn$_1$Ni$_4$ ZIF-8 at −1.13 V *vs.* the RHE, which is among the top values as listed in Table S8 (ESI†).

C-Zn$_1$Ni$_4$ ZIF-8 remains highly stable and shows a CO Faradaic efficiency of around 97.8% at −0.63 V (*vs.* the RHE) for 720 min in the CO_2-saturated 1 M $KHCO_3$ solution (Fig. 4a). The HRTEM images and XPS spectra of C-Zn$_1$Ni$_4$ ZIF-8 after the stability test (Fig. S19, ESI†) show that there is neither changes in morphology and chemical states, nor the formation of metal NPs. The X-ray absorption spectroscopy (XAS) measurements of the used electrode also reveal that the structure and the coordination state of the Ni species in C-Zn$_1$Ni$_4$ ZIF-8 remain unchanged (Fig. S20, ESI†). There were no dissolved nickel or zinc ions in the cathodic electrolyte after the stability test detected by ICP-OES analysis, confirming the high stability of C-Zn$_1$Ni$_4$ ZIF-8 under the CO_2RR conditions.

The critical role of Ni species towards the CO_2RR is highlighted by more C-Zn$_x$Ni$_y$ ZIF-8 samples prepared *via* pyrolysis in Ar at 900 °C for 4 h (Fig. S21–S24 and Tables S9–S13, ESI†) with a similar morphology and structure. High CO Faradaic efficiencies and current densities are also obtained over the pyrolysis products at 900 °C (Fig. S25, ESI†). In order to clarify the effect of Ni and Zn loadings in the catalysts on the CO current density, the six catalysts are divided into two groups. The Zn loadings in group 1 and 2 are 6.20–8.81 wt% and 2.91–3.29 wt%, respectively (Tables S2 and S9, ESI†). As shown in Fig. 4b, the CO current density increases with Ni loading in both groups. Compared with group 2 catalysts, a higher Zn loading results in a lower CO current density for group 1 catalysts even with a higher Ni loading, indicating the blocking of active sites by Zn species. When pyrolyzed at 900 °C for 4 h, less Zn species was evaporated thus resulting in a lower surface area (Table S13, ESI†) compared with their counterparts pyrolyzed at 1000 °C for 4 h

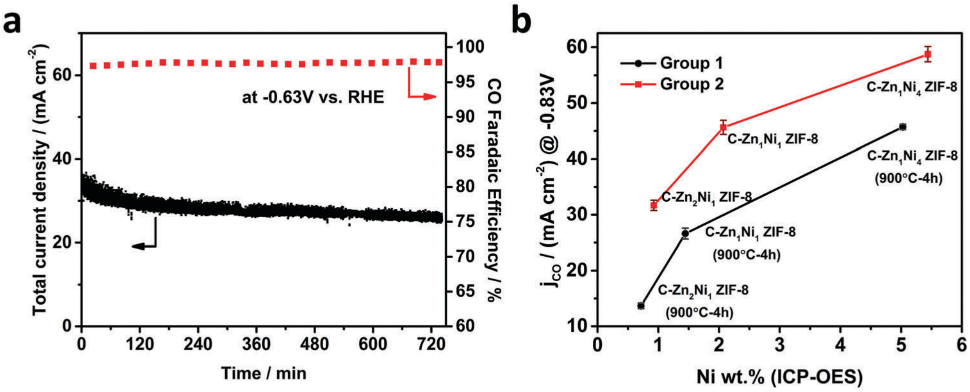

Fig. 4 Electrocatalytic performance of the CO_2RR over the catalysts in CO_2-saturated 1 M $KHCO_3$ solution with a catalyst loading of 2.0 ± 0.1 mg cm^{-2}. (a) Stability test of C-Zn_1Ni_4 ZIF-8 at −0.63 V *vs.* RHE, and (b) CO current density *versus* the content of Ni in C-Zn_xNi_y ZIF-8 at −0.83 V *vs.* RHE.

or at 900 °C for 10 h. Therefore, it is proposed that the coordinatively unsaturated Ni–N_x sites are the active sites for the CO_2RR and that the CO_2RR performance is strongly dependent on the exposure of active sites.

DFT calculations are performed to further understand the catalytic selectivity of the CO_2RR and the HER over Ni–N and Zn–N sites. Based on our XANES and EXAFS experimental characterization results for the Ni–N coordination number, we built

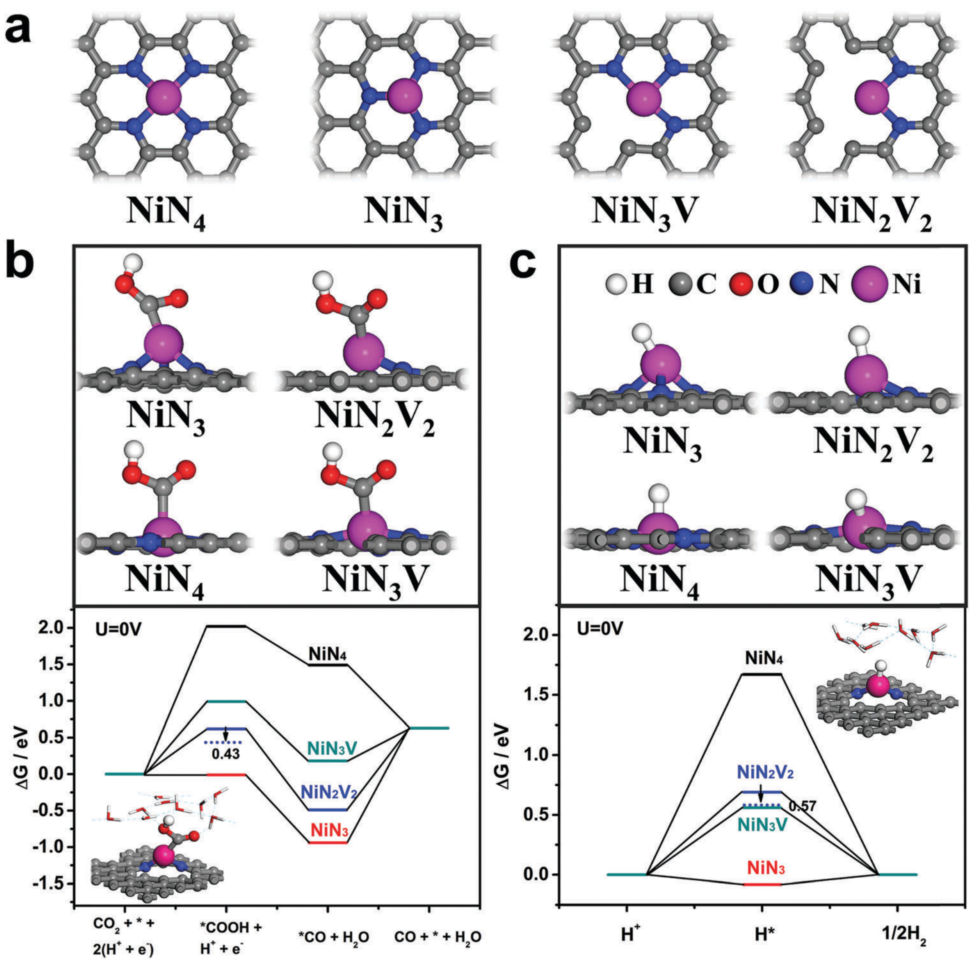

Fig. 5 DFT calculations. (a) Optimized atomic structures of different Ni–N structures with Ni atoms coordinated with 4 N atoms (NiN_4), 3 N atoms (NiN_3 and NiN_3V), 2 N atoms (NiN_2V_2). (b and c) Free energy diagrams with implicit (solid lines) and explicit (dashed lines) solvation effect corrections for the CO_2RR (b) and the HER (c) pathways on Ni sites of different Ni–N structures at 0 V. Optimized atomic structures for *COOH and *H intermediates adsorbed on Ni sites are shown at the top. Inset: *COOH and *H intermediates adsorbed on the NiN_2V_2 site with one water molecule layer to simulate the solvent environment. The white, grey, red, blue, and purple balls represent H, C, O, N, and Ni atoms, respectively.

a Ni–N–C embedded in the graphene plane model to simulate the active site structure. As shown in Fig. 5a, four Ni–N structures with Ni atoms coordinated with 4 N atoms (NiN_4), 3 N atoms (NiN_3 and NiN_3V) and 2 N atoms (NiN_2V_2) have been considered to represent different Ni–N coordination conditions, where V stands for coordination vacancy. The electroreduction of CO_2 into CO on metal active sites is generally considered as three elementary steps, consisting of the initial state (CO_2 molecule), adsorbed intermediate states (*COOH, *CO) and the terminal state (CO molecule).[24,25] Among these intermediates, the most important one is *COOH, the free energy of which reflects the CO_2RR activity from the point of view of limiting potential, while in addition, the desorption of *CO into the gas phase also affects the reactivity performance. As shown in Fig. 5b, the free energies of *COOH (G_{*COOH}) on coordinatively unsaturated NiN_3, NiN_3V and NiN_2V_2 are significantly lower than those on NiN_4, suggesting that the high CO_2RR activity originates from those coordinatively unsaturated Ni–N sites. After considering the effect of the applied electric potential, the thermodynamic reduction potential will be further decreased at the applied potential of −0.43 V (Fig. S26, ESI†).

The competition between the CO_2RR and the HER at the active sites can be investigated by comparing the free energies of *COOH (G_{*COOH}) and *H (G_{*H}).[26] From Fig. 5c, it can be inferred that *H blockage is relatively weak on NiN_3V and NiN_2V_2 structures. Especially for NiN_2V_2, G_{*COOH} (0.62 eV) is lower than G_{*H} (0.69 eV), which shows high selectivity for the CO_2RR. In contrast, *H is quite preferred to adsorb on NiN_3 (Fig. 5c), which leads to a predominantly HER process, and the desorption of *CO on NiN_3 is the most difficult among the four structures (Fig. 5b). In addition, the DFT calculations on Zn–N sites with the same structures (ZnN_4, ZnN_3, ZnN_3V and ZnN_2V_2) show that they have low selectivity for the CO_2RR (Fig. S27, ESI†), consistent with the inferior CO_2RR performance over C-ZIF-8 (Fig. 3a and b). Therefore, the structure of the active site is most likely NiN_2V_2 with a Ni–N coordination of 2, agreeing well with the XANES and EXAFS results (Fig. 2c and d, Table S4, ESI†). Moreover, the effect of the electrolyte has also been taken into consideration both by implicit correction (solid line in Fig. 5b and c) in the literature[24] and by adding solvent water molecules onto the surface as an explicit correction (dashed line in Fig. 5b and c). Taking the NiN_2V_2 structure as an example, G_{*COOH} and G_{*H} decrease to 0.43 eV and 0.57 eV by explicit correction, respectively, which is consistent with the result by implicit correction. A recent investigation proposes the active site structure to be NiN_3C, and a maximum CO Faradaic efficiency of 71.9% is reported.[8] Our DFT calculations show that NiN_2V_2 is much more active and selective for the CO_2RR than NiN_3C (Fig. S28, ESI†). Correspondingly, a maximum CO Faradaic efficiency of 98.0% is achieved over our Ni–N composite catalysts.

In summary, highly doped and coordinatively unsaturated Ni–N active sites within porous carbon demonstrate high selectivity and activity for the CO_2RR. CO Faradaic efficiencies of 92.0–98.0% have been achieved over a wide potential range of −0.53 to −1.03 V (*vs.* the RHE). The coordinatively unsaturated Ni–N sites exhibit a high intrinsic activity towards the CO_2RR, as confirmed by a high TOF of $10\,087 \pm 216\ h^{-1}$ for C-Zn_1Ni_4 ZIF-8. Besides, a maximum current density of $71.5 \pm 2.9\ mA\ cm^{-2}$ has been obtained at −1.03 V (*vs.* the RHE) over C-Zn_1Ni_4 ZIF-8. DFT calculations reveal that the CO_2RR occurs more easily than the HER over coordinatively unsaturated Ni–N sites, thus surmounting the constraints between the Faradaic efficiency and current density of the CO_2RR.

Conflicts of interest

There are no conflicts to declare.

Acknowledgements

We gratefully acknowledge financial support from the Ministry of Science and Technology of China (Grants 2016YFB0600901 and 2013CB933100), the National Natural Science Foundation of China (Grants 21573222 and 91545202), the Dalian Institute of Chemical Physics (Grant DICP DMTO201702), and the Strategic Priority Research Program of the Chinese Academy of Sciences (Grant No. XDB17020200). We thank Prof. Wen-Bin Cai at Fudan University, Prof. Zhangquan Peng at the Changchun Institute of Applied Chemistry, Chinese Academy of Sciences and Associate Prof. Linlin Yang at the Dalian Institute of Chemical Physics, Chinese Academy of Sciences for fruitful discussions. We thank staff at the BL14W1 beamline of the Shanghai Synchrotron Radiation Facility (SSRF) for their kind help during the XAFS measurements. G. X. Wang acknowledges the financial support from the CAS Youth Innovation Promotion (Grant No. 2015145).

Notes and references

1 D. D. Zhu, J. L. Liu and S. Z. Qiao, *Adv. Mater.*, 2016, **28**, 3423–3452.

2 Y. Hori, *Modern Aspects of Electrochemistry*, Springer, New York, 2008, vol. 42, ch. 3, pp. 89–189.

3 D. T. Whipple and P. J. A. Kenis, *J. Phys. Chem. Lett.*, 2010, **1**, 3451–3458.

4 B. Khezri, A. C. Fisher and M. Pumera, *J. Mater. Chem. A*, 2017, **5**, 8230–8246.

5 Q. Lu, J. Rosen, Y. Zhou, G. S. Hutchings, Y. C. Kimmel, J. G. Chen and F. Jiao, *Nat. Commun.*, 2014, **5**, 3242–3247.

6 Y. Chen, C. W. Li and M. W. Kanan, *J. Am. Chem. Soc.*, 2012, **134**, 19969–19972.

7 T. N. Huan, N. Ranjbar, G. Rousse, M. Sougrati, A. Zitolo, V. Mougel, F. Jaouen and M. Fontecave, *ACS Catal.*, 2017, **7**, 1520–1525.

8 C. Zhao, X. Dai, T. Yao, W. Chen, X. Wang, J. Wang, J. Yang, S. Wei, Y. Wu and Y. Li, *J. Am. Chem. Soc.*, 2017, **139**, 8078–8081.

9 P. Su, K. Iwase, S. Nakanishi, K. Hashimoto and K. Kamiya, *Small*, 2016, **12**, 6083–6089.

10 A. S. Varela, N. R. Sahraie, J. Steinberg, W. Ju, H. S. Oh and P. Strasser, *Angew. Chem., Int. Ed.*, 2015, **54**, 10758–10762.

11 Y. Ye, F. Cai, H. Li, H. Wu, G. Wang, Y. Li, S. Miao, S. Xie, R. Si, J. Wang and X. Bao, *Nano Energy*, 2017, **38**, 281–289.

12 W. Ju, A. Bagger, G. P. Hao, A. S. Varela, I. Sinev, V. Bon, B. Roldan Cuenya, S. Kaskel, J. Rossmeisl and P. Strasser, *Nat. Commun.*, 2017, **8**, 944.

13 R. Li, X. Ren, X. Feng, X. Li, C. Hu and B. Wang, *Chem. Commun.*, 2014, **50**, 6894–6897.

14 W. Liu, L. Zhang, W. Yan, X. Liu, X. Yang, S. Miao, W. Wang, A. Wang and T. Zhang, *Chem. Sci.*, 2016, **7**, 5758–5764.

15 L. Sun, C. Yan, Y. Chen, H. Wang and Q. Wang, *J. Non-Cryst. Solids*, 2012, **358**, 2723–2726.

16 P. Yin, T. Yao, Y. Wu, L. Zheng, Y. Lin, W. Liu, H. Ju, J. Zhu, X. Hong, Z. Deng, G. Zhou, S. Wei and Y. Li, *Angew. Chem., Int. Ed.*, 2016, **55**, 10800–10805.

17 Y. Goto, K. Taniguchi, T. Omata, S. Otsuka-Yao-Matsuo, N. Ohashi, S. Ueda, H. Yoshikawa, Y. Yamashita, H. Oohashi and K. Kobayashi, *Chem. Mater.*, 2008, **20**, 4156–4160.

18 F. Petraki, V. Papaefthimiou and S. Kennou, *Org. Electron.*, 2007, **8**, 522–528.

19 Q. Lai, L. Zheng, Y. Liang, J. He, J. Zhao and J. Chen, *ACS Catal.*, 2017, **7**, 1655–1663.

20 N. R. Sahraie, U. I. Kramm, J. Steinberg, Y. Zhang, A. Thomas, T. Reier, J.-P. Paraknowitsch and P. Strasser, *Nat. Commun.*, 2015, **6**, 8618–8626.

21 L. Ottaviano, S. Di Nardo, L. Lozzi, M. Passacantando, P. Picozzi and S. Santucci, *Surf. Sci.*, 1997, **373**, 318–332.

22 L. A. Avakyan, A. S. Manukyan, A. A. Mirzakhanyan, E. G. Sharoyan, Y. V. Zubavichus, A. L. Trigub, N. A. Kolpacheva and L. A. Bugaev, *Opt. Spectrosc.*, 2013, **114**, 347–352.

23 N. A. Kolpacheva, L. A. Avakyan, A. S. Manukyan, A. A. Mirzakhanyan, E. G. Sharoyan, V. V. Pryadchenko, Y. V. Zubavichus, A. L. Trigub, A. G. Fedorenko and L. A. Bugaev, *Phys. Solid State*, 2016, **58**, 1004–1010.

24 A. A. Peterson, F. Abild-Pedersen, F. Studt, J. Rossmeisl and J. K. Nørskov, *Energy Environ. Sci.*, 2010, **3**, 1311–1315.

25 X. Liu, J. Xiao, H. Peng, X. Hong, K. Chan and J. K. Nørskov, *Nat. Commun.*, 2017, **8**, 15438–15444.

26 V. Tripkovic, M. Vanin, M. Karamad, M. E. Bjorketun, K. W. Jacobsen, K. S. Thygesen and J. Rossmeisl, *J. Phys. Chem. C*, 2013, **117**, 9187–9195.